Petroleum Science 22 (2025) 3447–3460

Contents lists available at ScienceDirect

Petroleum Science

journal homepage: www.keaipublishing.com/en/journals/petroleum-science

Original Paper

Catalyst deactivation model involving autocatalytic effect for the residue hydrotreating process

Zhong-Huo Deng [*], Rong Shi, Liang Ren, Xin-Peng Nie, Qiang Fang, Zhen Wang, Wei Han [**], Li-Shun Dai

Sinopec Research Institute of Petroleum Processing Co. Ltd., Beijing, 100083, China

ARTICLE INFO

Article history:
Received 4 December 2023
Received in revised form
22 July 2024
Accepted 29 April 2025
Available online 9 May 2025

Edited by Min Li

Keywords:
Residual oil hydrotreating
Catalyst deactivation
Autocatalytic effect
Deactivation model

ABSTRACT

Autocatalysis from the by-product metal sulfides plays a critical role in the residual oil hydrotreating (RHT) process. However, it has not been considered to build the catalyst deactivation models, which probably is one important reason that the widely used S-type deactivation models are inaccurate in predicting some RHT processes' deactivation profiles. A three-stage catalyst deactivation model was first developed to fill this gap based on the mechanism inferred from the experimental and literature data. This model accounts for active site formation from by-product metal sulfides, deactivation due to active site coverage by coke formation and metal deposition, active site poisoning by highly-adsorbed species, active phase sintering, and diffusion resistance from the pore blockage at the same time, resulting in a function of dimensionless metals-on-catalyst. Then, the effectiveness of the proposed model was evaluated using the industrial data of an RHT unit and the experimental data from the literature, either in combination with reaction kinetics or independently. Results showed that RHT processes with clear autocatalytic effects may display different types of deactivation profiles from the traditional "S" shape. However, the proposed model was able to accurately track the entire deactivation curve of the RHT process and well predict the product properties. This approach yields valuable insights into the intricate autocatalytic effect that remarkably contributes to the performance modification of RHT catalysts. It is highly recommended that further research should be conducted on this topic, as it shows great potential to significantly advance catalyst and process development.

1. Introduction

Residual oil hydrotreating (RHT) plays a critical role in refining processes, as it eliminates impurities like sulfur, nitrogen, nickel, and vanadium from residual oils prior to their utilization in the downstream production of transportation fuels, light olefins, or low-sulfur coke (Chehadeh et al., 2023; Deng et al., 2022; Sahu et al., 2015; Zhao et al., 2020). The most widely used RHT process is the trickle bed reactor, which is highly efficient, cost-effective, and easy to operate (Kressmann et al., 1998). However, the catalysts employed in this process are prone to rapid deactivation due to the metal deposition, coke formation, and the resulting reduced surface area and clogged pores (Furimsky and Massoth, 1999; Rodríguez et al., 2018). As a result, the operating cycle of an RHT unit is typically only 1–2 years, much shorter than that of downstream processes (e.g. that of fluid catalytic cracking is generally 3–4 years). Therefore, either extending or accurately predicting the operating cycle of the RHT process is crucial to optimize and improve the efficiency of the refining process (Furimsky and Massoth, 1999; Rodríguez et al., 2018; Sie, 2001).

To extend the operational life of the RHT process, our team has developed highly stable RHT catalysts. Using these catalysts, some interesting phenomena known as autocatalysis have been observed in certain experimental tests and industrial applications. Autocatalysis refers to a chemical reaction that is catalyzed by its own products (Plasson et al., 2011). During the RHT process, the by-product metal sulfides like VMoS, Ni_xS_y, V_mS_n, etc. are capable of catalyzing hydrogenation reactions, leading to observable

---

[*] Corresponding author.

[**] Corresponding author.

E-mail addresses: dengzh.ripp@sinopec.com (Z.-H. Deng), hanwei.ripp@sinopec.com (W. Han).

Peer review under the responsibility of China University of Petroleum (Beijing).

https://doi.org/10.1016/j.petsci.2025.04.031

autocatalysis in some cases (Al-Dalama et al., 2014; Bahzad and Kam, 2009; Dejonghe et al., 1990; Filby and Branthaver, 1987; Hubaut, 2007; Jia et al., 2016; Marafi et al., 2008, 2010). Notably, increasing the amount of deposited vanadium on the bare support up to 10% by weight resulted in an increase in hydrogenation activity (Filby and Branthaver, 1987), while other experiments using feedstocks with high or ultra-high metal content showed clear autocatalytic effects during the early stable stage, lasting for hundreds of hours (Bahzad and Kam, 2009; Marafi et al., 2008). In one experiment, stepwise changes in temperature between 360 and 405 °C confirmed the presence of autocatalysis, as the higher HDS rate during the second 360 °C test may only be the result of an autocatalytic effect (Al-Dalama et al., 2014). Furthermore, it was found that the hydrotreating activity of the deposited metal sulfides depends on the type of initial catalyst and is lower than that of NiMoS or CoMoS (Dejonghe et al., 1990; Hubaut, 2007). Therefore, whether observable or not, autocatalysis is commonly involved in the RHT process and may be at least partially responsible for the apparent deactivation results (Marafi et al., 2010). In other words, this autocatalytic effect plays a critical role in the RHT process, and a significant, long-lasting autocatalytic effect would greatly improve the product properties and prolong the operating cycle.

Despite the positive effect of the autocatalysis phenomenon, it meanwhile actually increases the difficulty of fully understanding and accurately modeling/predicting the RHT process. In fact, establishing a suitable catalyst deactivation model for the RHT process has always been a great challenge because of the following reasons. Firstly, the deactivation mechanism of hydrotreating catalysts is highly complex, mainly involving active site coverage by coke and metal deposition, active site poisoning by highly-adsorbed species, diffusion resistance induced by pore mouth blockage, active phase sintering, etc. (Furimsky and Massoth, 1999). Secondly, while coke formation and metal deposition have been identified as the primary causes of RHT catalyst deactivation, their manifestation is highly influenced by a wide range of factors, such as catalyst characteristics, catalyst grading strategies, feedstock properties, and reaction conditions (Al-Mutairi and Marafi, 2012; Kohli et al., 2016; Maity et al., 2007; Marafi and Stanislaus, 2001; Morales–Leal et al., 2023; Oyekunle et al., 2005; Rodríguez et al., 2018; Sámano et al., 2020a; Seki and Yoshimoto, 2001; Takahashi et al., 2005; Torres-Mancera et al., 2014, 2018). Furthermore, the impact of metal deposition and coke formation on catalyst deactivation evolves dynamically over time-on-stream (TOS), exhibiting distinct deactivation stages. Typically, this progression includes a rapid fouling stage caused by coke formation at the start of run (SOR), a gradual poisoning stage due to metal deposition at the middle of run (MOR), and a final rapid decline stage resulting from the diffusion resistance from the pore blockage induced by metal deposition and coke formation at the end of run (EOR) (Elizalde and Ancheyta, 2014a; Jurado and Ancheyta, 2022). Finally, it is important to note the significant impact of the autocatalytic effect of deposited metal sulfides on the catalyst deactivation profile, as mentioned above (Al-Dalama et al., 2014; Filby and Branthaver, 1987; Marafi et al., 2008, 2010). In short, all these aspects should be carefully identified and considered before establishing a catalyst deactivation model for the RHT process (Marafi et al., 2010; Rodríguez et al., 2018).

Anyway, researchers have made significant progress in developing catalyst deactivation models for the RHT process. Most of these models focus on mechanisms involving metal deposition and coke formation, but some are only applicable to certain stages of the process, such as the SOR stage and/or the MOR stage (Centeno et al., 2012; Chen et al., 2022; Jiang et al., 2010; Jurado et al., 2024; Martínez and Ancheyta, 2012). This limitation makes it difficult to simulate the entire deactivation process. Additionally, some models correlate the activity with TOS rather than the reacting species (Chen et al., 2022; Elizalde and Ancheyta, 2014b; Idei et al., 1995, 1998, 2003), which may further limit their flexibility. Notably, a few models consider the impact of all three stages of catalyst deactivation (Al Bazzaz et al., 2015; Elizalde and Ancheyta, 2014a, 2014b; Idei et al., 1995, 1998, 2003; Jurado and Ancheyta, 2022; Kam et al., 2005; Khang and Mosby, 1986; Toulhoat et al., 2005; Zhang et al., 2021), as well as some important issues such as the morphology of metal deposits in the catalyst pore (Melkote and Jensen, 1989; Zhang and Seaton, 1996), the influence of reaction conditions (Kam et al., 2005; Toulhoat et al., 2005), and the impact of feedstock and catalyst properties (Chehadeh et al., 2018, 2021; Zhang and Seaton, 1996). In particular, Idei et al., (1995, 1998, 2003) have proposed a three-stage catalyst deactivation model for the RHT process that links the active site coverage and diffusion resistance to TOS. Elizalde and Ancheyta (2014b) have demonstrated the model's accuracy by providing a detailed parameter estimation procedure based on experimental data. In addition, Elizalde and Ancheyta (2014c) have conducted a simulation of catalyst deactivation in atmospheric residue hydrocracking. Their model includes active site coverage and pore mouth constriction, which accurately reflects the trend of hydrocracking in a different format. Rodríguez et al. (2018) have extensively analyzed many of these models and provided valuable recommendations for the development of more comprehensive deactivation models. However, it should be noted that these models do not account for the autocatalytic effect and typically show S-shaped deactivation profiles, with few exceptions (Marafi et al., 2010; Rodríguez et al., 2018). This may be because the clear autocatalytic effect has rarely been reported, and the traditional S-type models are accurate enough to simulate the conventional RHT process. With the advancement of highly stable catalysts, more and more clear autocatalytic effects have been shown in the RHT process. It is unfortunate that the widely used S-type deactivation models have been shown to be inaccurate in predicting the deactivation profile during a process with a clear autocatalytic effect, for the simple reason that these models suggest a decreasing activity profile with increasing TOS, whereas the actual activity would increase at some stages. The lack of consideration for the autocatalytic effect in the catalyst deactivation model could lead to inappropriate operation guidelines and inaccurate predictions of catalyst life for the RHT process. For example, to achieve stable product properties in the RHT process, the S-type models would suggest an increasing reaction temperature with increasing TOS, whereas for the clear autocatalysis situation, either increasing or decreasing the reaction temperature during operation may be required. Therefore, in order to address these issues, it is crucial to investigate the autocatalytic mechanism during this process and incorporate it into the catalyst deactivation model (Marafi et al., 2010).

Herein, by involving the autocatalytic effect for the first time, we developed a new model to accurately simulate the catalyst deactivation profile during the RHT process. To achieve this, we proposed a deactivation mechanism after thoroughly discussing different catalyst deactivation profiles using experimental and literature data. Then we developed a three-stage deactivation model by introducing two functions to represent the variation of active sites and the resulting diffusion resistance, respectively. The resulting model depends on dimensionless metals-on-catalyst (MOC), which accounts for the loss of active sites due to active site coverage, the active site poisoning and active phase sintering, the generation of active sites by the autocatalytic effect originating from the by-product metal sulfides, as well as the diffusion resistance due to the pore blockage of the catalysts. Furthermore, to demonstrate the adaptability and flexibility of the proposed model, we simulated the deactivation of various hydrogenation reactions using industrial and literature data with the three-stage information. Overall, our model provides a more comprehensive understanding of catalyst deactivation during the RHT process.

2. Deactivation model

2.1. Model assumptions

The proposed catalyst deactivation model was modified from a three-stage model proposed by Idei et al., which originally considered the deactivation mechanisms of active site loss and diffusion resistance (Idei et al., 1995, 1998, 2003). To include autocatalytic effects and improve its flexibility, three assumptions were made as follows:

I. Deactivation mechanisms include active site loss, active site formation, and diffusion resistance. Specifically, active site loss can be due to active site coverage by coke and metal species, active site poisoning by highly adsorbed species, active phase sintering, etc.; active site creation can only be due to the by-product metal sulfides, while diffusion resistance can be originated from the pore blockage by coke formation and metal deposition. Moreover, all these aspects could be correlated as a function of metal deposition.

II. There are two types of hydrogenation active sites, type I and type II. Both types of active sites have the same hydrogenation activity, but degrade independently of each other at two different rates, with type I degrading faster than type II, and despite the many deactivation mechanisms, the loss rate of each active site is proportional to its concentration at the first reaction order.

III. The active sites generated by the deposited metal sulfides could be treated as equivalent to type II active sites, i.e., they have the same activity and deactivation rate as type II active sites. Meanwhile, the rate of active site generation by the autocatalytic effect would decrease with increasing deposited metals.

2.2. Deactivation model greatly correlated with the change of active sites

If M and M_0 are the concentration of MOC and the maximum concentration of MOC, respectively, the dimensionless MOC is present as:

$$\tau = \frac{M}{M_0} \tag{1}$$

Given that type I and type II active sites degrade independently of one another and that their loss rates are proportional to their concentrations, if N, N_1, and N_2 are the concentrations of the total active sites, type I active sites, and type II active sites, respectively, the loss rate of type I active sites could be expressed as follows:

$$\frac{\mathrm{d}N_1}{\mathrm{d}\tau} = -\alpha_1 N_1 \tag{2}$$

The initial condition at $\tau = 0$ for Eq. (2) is:

$$N_1^0 = cN^0 \tag{3}$$

where N^0 is the initial concentration of the total active sites, and c is the initial fraction of type I active sites, which is defined as:

$$c = \frac{N_1^0}{N^0} \tag{4}$$

Thus, with proper substitution of the initial condition, the solution for Eq. (2) is:

$$N_1 = cN^0 \mathrm{e}^{-\alpha_1 \tau} \tag{5}$$

For type II active sites, the variation of concentration could be written as:

$$\frac{\mathrm{d}N_2}{\mathrm{d}\tau} = p_1 \mathrm{e}^{-\alpha_2 \tau} - \alpha_2 N_2 \tag{6}$$

where the first term proposes that the concentration of the equivalent type II active sites generated by the deposited metal sulfides would decrease with increasing deposited metals, while the second term suggests that the equivalent type II active sites deactivate by the same mechanism as type II active sites.

The initial condition at $\tau = 0$ for Eq. (6) is:

$$N_2^0 = (1-c)N^0 \tag{7}$$

Then, with proper substitution of the initial condition, the solution for Eq. (6) is:

$$N_2 = \left((1-c)N^0 + p_1 \tau\right)\mathrm{e}^{-\alpha_2 \tau} \tag{8}$$

The deactivation function φ_A due to the variation of active sites is defined as:

$$\varphi_A = \frac{N}{N^0} = \frac{N_1 + N_2}{N^0} \tag{9}$$

Through substituting Eqs. (1), (5) and (8) into Eq. (9) and using a new parameter p to represent p_1/N^0, we get:

$$\varphi_A = c\mathrm{e}^{-\alpha_1 \frac{M}{M_0}} + \left(1 - c + p\frac{M}{M_0}\right)\mathrm{e}^{-\alpha_2 \frac{M}{M_0}} \tag{10}$$

2.3. The deactivation model greatly correlated with the diffusion resistance

The deactivation from the diffusion resistance caused by the coke formation and metal deposition could be calculated with the initial effectiveness factor η_0 and the effectiveness factor η_τ at a given τ as follows (Elizalde and Ancheyta, 2014b; Idei et al., 1998):

$$\varphi_D = \frac{\eta_\tau}{\eta_0} \tag{11}$$

Assuming that the catalyst particle could be considered as spherical with an adequate equivalent diameter, the effectiveness factor can be mathematically correlated with Thiele modulus by the following equation (Elizalde and Ancheyta, 2014b; Idei et al., 1998):

$$\eta = \frac{1}{\sqrt{1+\phi^2}} \tag{12}$$

Substituting Eq. (12) into Eq. (11) gets:

$$\varphi_D = \frac{1}{\eta_0}\frac{1}{\sqrt{1+\phi_\tau^2}} \tag{13}$$

The Thiele modulus for first order reaction kinetics is written as:

$$\phi = \sqrt{k/D} \tag{14}$$

Dividing the initial Thiele modulus by the Thiele modulus at a given τ gives:

$$\frac{\phi_0}{\phi_\tau} = \sqrt{D_\tau/D_0} \tag{15}$$

The restrictive diffusion could be expressed as (Beck and Schultz, 1972; Marafi et al., 2010):

$$D = A(1-\lambda)^4 \tag{16}$$

where A is the proportionality constant and λ is the ratio of the reactant radius r_m to the catalyst pore radius r.

Thus, dividing the diffusion coefficient at a given τ by the initial diffusion coefficient, the result will be:

$$\frac{D_\tau}{D_0} = \frac{(1-\lambda_\tau)^4}{(1-\lambda_0)^4} \tag{17}$$

Assuming that the metal sulfides are uniformly deposited on the walls of cylindrical pores, then at a given τ, the mass balance could be written as:

$$M = \rho_\mathrm{M} L\pi\left(r_0^2 - r_\tau^2\right) \tag{18}$$

Since diffusion coefficient reduces to zero when $r_\tau = r_\mathrm{m}$, the maximum amount of metal deposition is calculated by:

$$M_0 = \rho_\mathrm{M} L\pi\left(r_0^2 - r_\mathrm{m}^2\right) \tag{19}$$

From Eqs. (18) and (19), r_τ could be calculated as:

$$r_\tau = \sqrt{r_0^2 - \frac{M}{M_0}\left(r_0^2 - r_\mathrm{m}^2\right)} \tag{20}$$

Setting r_0 as unity, Eq. (20) could be rearranged as:

$$r_\tau = \sqrt{1 - \frac{M}{M_0}\left(1-\lambda_0^2\right)} \tag{21}$$

Substituting Eq. (21) into Eq. (17), we can obtain:

$$\frac{D_\tau}{D_0} = \frac{\left[1 - \frac{\lambda_0}{\sqrt{1-\frac{M}{M_0}\left(1-\lambda_0^2\right)}}\right]^4}{(1-\lambda_0)^4} \tag{22}$$

By substituting Eq. (15) into Eq. (12), Eq. (23) can be derived as:

$$\varphi_D = \frac{1}{\eta_0^2 + \frac{\eta_0^2\phi_0^2}{D_\tau/D_0}} \tag{23}$$

Thus, by substituting Eqs. (12) and (22) into Eq. (23), we get:

$$\varphi_{D1} = \frac{1}{\eta_0^2 + \frac{\left(1-\eta_0^2\right)(1-\lambda_0)^4}{\left[1-\frac{\lambda_0}{\sqrt{1-\frac{M}{M_0}\left(1-\lambda_0^2\right)}}\right]^4}} \tag{24}$$

Mathematically, within reasonable limits, Eq. (24) could be approximated by function with fewer parameters as shown below:

$$\varphi_{D2} = \frac{\arctan\left(d\left(1-\frac{M}{M_0}\right)\right)}{\arctan d} \tag{25}$$

where d is a regressed parameter.

2.4. The complete deactivation models

The complete deactivation model could actually be split into two mechanisms, e.g., the deactivation due to active site modification and deactivation due to diffusion resistance. It has been proposed that the deactivation due to two causes can be calculated as follows (Corella and Monzón, 1988; Trueba et al., 2023):

$$\varphi = \varphi_A \varphi_D \tag{26}$$

Substituting Eqs. (24) and (25) into Eq. (26) separately, we obtain the final deactivation models as Eqs. (27) and (28):

$$\varphi_1 = \frac{c\mathrm{e}^{-\alpha_1\frac{M}{M_0}} + \left(1-c+p\frac{M}{M_0}\right)\mathrm{e}^{-\alpha_2\frac{M}{M_0}}}{\eta_0^2 + \frac{\left(1-\eta_0^2\right)(1-\lambda_0)^4}{\left(1-\sqrt{1-\frac{M}{M_0}\left(1-\lambda_0^2\right)}\right)^4}} \tag{27}$$

$$\varphi_2 = \left(c\mathrm{e}^{-\alpha_1\frac{M}{M_0}} + \left(1-c+p\frac{M}{M_0}\right)\mathrm{e}^{-\alpha_2\frac{M}{M_0}}\right)\left(\frac{\arctan\left(d\left(1-\frac{M}{M_0}\right)\right)}{\arctan d}\right) \tag{28}$$

In nonlinear Eqs. (27) and (28), there are seven parameters (α_1, α_2, c, p, η_0, λ_0, M_0) and six parameters (α_1, α_2, c, p, d, M_0) respectively, which may be determined by using catalyst characteristics, reaction conditions, feedstock and product properties, and other information.

Before these calculations, the MOC could be calculated by the following expression:

$$M_i = \sum_{i=1}^{m} \frac{t_i F_\mathrm{L} \rho_\mathrm{L}}{10^9 V_\mathrm{cat}}\left(C_\mathrm{Ni,f} + C_\mathrm{V,f} - C_\mathrm{Ni,p} - C_\mathrm{V,p}\right) \tag{29}$$

The initial effectiveness factor η_0 could be obtained by dividing the apparent rate constant by the intrinsic rate constant in experiments with different catalyst sizes (Elizalde and Ancheyta, 2014b; Perego and Peratello, 1999). Theoretically, the initial ratio of the reactant radius to the catalyst pore radius λ_0 could be estimated by dividing the hydrodynamic radius of the feedstock by the average pore radius of the catalyst. However, determining a representative molecular for different hydrogenation reactions is a great challenge as the distribution of impurities varies based on the impurity kind and feedstock source, although the hydrodynamic radius of the feedstock can be correlated to molecular weight according to several studies (Barré et al., 2008; Chen et al., 2011, 2015). As a result, we recommend that the parameters of both Eqs. (27) and (28) can be obtained by nonlinear regression with careful constraints within reasonable limits until a reliable estimation method is established for λ_0.

In this study, when simulating experimental data from the literature (Marafi et al., 2008), as the normalized reaction constants were given, the experimental deactivation data was calculated by:

$$\varphi^{\text{exp}} = \frac{k_\tau}{k_0} \tag{30}$$

Then, the parameters in Eq. (28) were solved by the following minimum function:

$$\text{function} = \min \sum_{i=1}^{m} \left(\varphi_i^{\text{cal}} - \varphi_i^{\text{exp}}\right)^2 \tag{31}$$

2.5. Coupling deactivation model with reaction kinetics

The data from the industrial RHT unit was evaluated using n-class reaction kinetics for HDS, carbon-residue reduction (HDCCR), hydrodenickelation (HDNi), and hydrodevanadization (HDV). The following equation was used to calculate the impurity concentration in the product when $n = 1$:

$$C_{\text{p}} = C_{\text{f}} \exp\left[-A_0\varphi \exp\left(-\frac{E}{RT}\right)\frac{1}{\text{LHSV}}\right] \tag{32}$$

where C_{f}, C_{p}, A_0, E, and R are the impurity concentration in the feed, the impurity concentration in the product, the initial pre-exponential factor, the apparent activation energy, and the gas constant, respectively.

When $n \neq 1$, Eq. (33) was used to calculate the impurity concentration in the product as below:

$$C_{\text{p}} = \left[C_{\text{f}}^{1-n} + (n-1)A_0\varphi \exp\left(-\frac{E}{RT}\right)\frac{1}{\text{LHSV}}\right]^{\frac{1}{1-n}} \tag{33}$$

If the reaction temperature remains unchanged, Eq. (33) can be simplified as below:

$$C_{\text{p}} = \left[C_{\text{f}}^{1-n} + (n-1)k_\tau\frac{1}{\text{LHSV}}\right]^{\frac{1}{1-n}} \tag{34}$$

When simulating the industrial data, Eq. (33) was solved by nonlinear regression with the aim of minimizing the residual between simulation and industrial data as shown below:

$$\text{function} = \min(\text{SSE}) = \min \sum_{i=1}^{m} \left(C_i^{\text{cal}} - C_i^{\text{ind}}\right)^2 \tag{35}$$

3. Experimental

To study the autocatalytic mechanism during the RHT process, tests using highly stable catalysts were carried out in a fixed bed reactor, the details of which have been reported previously (Zhao et al., 2021). The feedstocks used in these tests were two mixed high-sulfur Middle East residual oils and a low-sulfur residual oil, the characteristics of which are shown in Table 1.

Three commercial Alumina-supported NiMo catalysts were used in the tests, the properties of which are shown in Table 2. After being loaded as shown in Table 3, the catalysts were pre-sulfided using the same protocol described elsewhere (Zhao et al., 2021). After sulfidation, the RHT tests were carried out under different reaction conditions as shown in Table 3. It could be seen that the tests were carried out with a constant reaction temperature.

During these tests, the product properties were analyzed every day or two days to obtain the catalyst deactivation information. As the reaction temperatures remained unchanged during these tests, the activity coefficient or deactivation function φ_{HDS} was calculated using Eqs. (30) and (34). The HDS reaction orders n for Cases A to D were 1.83, 1.69, 2.14 and 2.15 respectively. This information was determined in previous work and is available in Figs. S1–S4 in the Supporting Information.

4. Results and discussion

4.1. The autocatalytic mechanism in the RHT process

Fig. 1 illustrates the variation of HDS, HDCCR, HDNi, and HDV ratios with TOS for Catalyst A. The results indicate a distinct deviation from the conventional "S-type" deactivation profile of RHT catalysts, where the impurity removal ratios slightly increased at first with increasing TOS before decreasing at different levels. Similar results were observed in the RHT process when treating a feedstock with ultra-high metal content (Marafi et al., 2008). Such behaviors offer compelling evidence of autocatalysis phenomenon during the RHT processes, which can only be attributed to the by-product metal sulfides with hydrotreating potentials (Al-Dalama et al., 2014; Bahzad and Kam, 2009; Filby and Branthaver, 1987; Marafi et al., 2008, 2010). Interestingly, the autocatalytic effect on different hydrogenation reactions is somewhat different. Specifically, the effect was most pronounced on the HDS reaction, followed by HDCCR, HDV, and HDNi. Comparable results were reported in the literatures (Al-Dalama et al., 2014; Filby and Branthaver, 1987; Marafi et al., 2010). Although direct evidence is

Table 1
Properties of the feedstocks.

Properties	Feed A	Feed B	Feed C
ρ^{20}, g/mL	0.9812	0.9916	0.9643
ν^{100}, mm^2/s	80.4	61.4	112.0
CCR, wt%	13.04	11.15	9.39
C, wt%	84.28	84.15	86.23
H, wt%	10.96	10.59	11.65
S, wt%	4.42	4.95	1.41
N, wt%	0.23	0.22	0.36
Ni, μg/g	23.8	21.7	29.0
V, μg/g	83.0	78.4	27.0
Saturates, wt%	29.0	26.2	33.1
Aromatics, wt%	46.1	50.4	37.6
Resins, wt%	19.3	18.5	27.5
Asphaltenes, wt%	5.6	4.9	1.8

Table 2
Physical properties of the catalysts used in the RHT process.

Properties	Catalyst A	Catalyst B	Catalyst C
Diameter, mesh	16–20	16–20	16–20
Surface area, m^2/g	140–180	100–130	150–190
Pore volume, mL/g	0.5–0.7	0.6–0.8	0.4–0.6
Active species	NiMo	NiMo	NiMo
Average pore diameter, nm	12.5–18.0	18.6–27.5	9.0–15.0
Acid type	Lewis acid	Lewis acid	Lewis acid

Table 3
Catalyst, feed and operating conditions for the RHT process.

Case	Case A	Case B	Case C	Case D
Catalyst	Catalyst A	Catalyst B	Catalyst C	Catalyst C
Feed	Feed A	Feed A	Feed B	Feed C
Temperature, °C	380	390	380	380
Hydrogen pressure, MPa	14	14	14	14
LHSV, h^{-1}	0.5	0.8–1.0	0.5	0.5
$V(H_2)/V(Oil)$, mL/mL	600	600	600	600
TOS, d	62	114	42	24

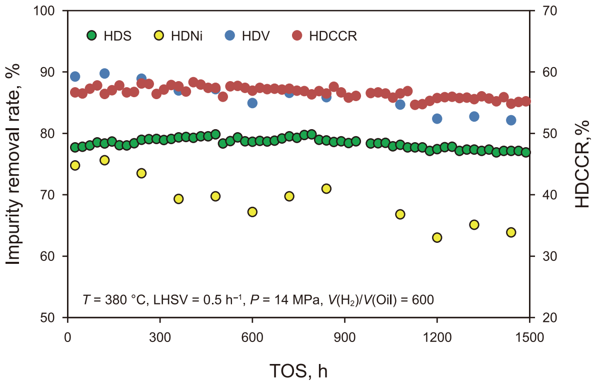

Fig. 1. Plots of impurity removal rates as a function of TOS over Catalyst A.

lacking, it is plausible to assume that the controlling factors of these reactions are distinct. For example, HDS and HDCCR may be more sensitive to the concentration of active sites, whereas HDV and HDNi may be more sensitive to the diffusion resistance existing in catalyst pores.

Furthermore, our investigations, along with the literature data (Bahzad and Kam, 2009; Dejonghe et al., 1990; Marafi et al., 2008), have revealed that the autocatalytic effect on the hydrotreating reaction was found to be dependent on the catalyst systems, feed properties and the reaction conditions. In Fig. 2(a), the deactivation profiles of Catalyst A, Catalyst B, and a previously reported catalyst system for hydrotreating atmospheric residue from Kuwait Export Crude (KEC-AR) (Marafi et al., 2008) are displayed. It could be seen that, unlike the deactivation profile of Catalyst A, there was another deactivation profile where the activity coefficient first dropped rapidly, followed by a slight or strong increase, before declining to a certain rate. In Fig. 2(b) it is shown that, although using the same catalyst and under the same reaction conditions, the catalyst activity coefficient using Feed B increased with increasing MOC before decreasing, while the catalyst activity coefficient using Feed C remained almost unchanged during the experimental period (about 576 h). These phenomena confirm that catalyst deactivation profiles with a clear autocatalytic effect could be quite different for different catalyst systems, feed properties and reaction conditions. These factors may influence both autocatalysis and other deactivation mechanisms. Interestingly, for these deactivation profiles, the transition point from higher to lower activity occurred in the MOR stage, where the catalyst is usually gradually deactivated, indicating that the transition ratio from deposited metal sulfides to active sites may decrease with increasing MOC.

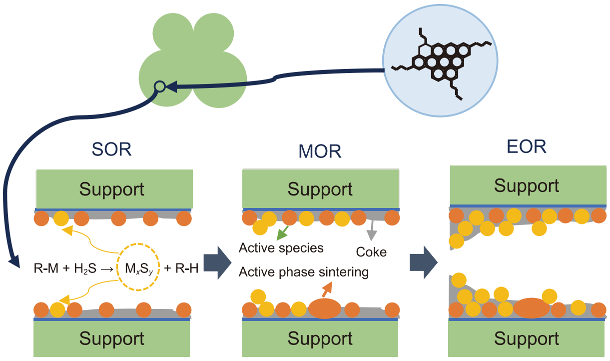

Fig. 3. Schematic diagram of the deactivation mechanism of RHT catalyst when involving the autocatalytic effect.

To deepen the understanding of these phenomena, we proposed a potential catalyst deactivation mechanism for the RHT process, as illustrated in Fig. 3. The activity of a catalyst can be influenced by several factors. Firstly, due to active site coverage by coke formation and metal deposition, active site poisoning by highly-adsorbed species and active phase sintering, and etc. (Furimsky and Massoth, 1999), active sites decrease. Secondly, the formation of new active sites from the by-product metal sulfides (Al-Dalama et al., 2014; Bahzad and Kam, 2009; Dejonghe et al., 1990; Filby and Branthaver, 1987; Hubaut, 2007; Marafi et al., 2008, 2010). Finally, due to the pore blocking by coke formation and metal deposition, the ever-increasing diffusion resistance further reduces the catalytic activity (Idei et al., 1995, 1998, 2003; Marafi et al., 2010; Rodríguez et al., 2018). During the SOR stage, the coke formation derived catalyst deactivation typically dominates, as observed in the case of Catalysts B as shown in Fig. 2. However, well-designed catalysts like Catalyst A and Catalyst C can improve

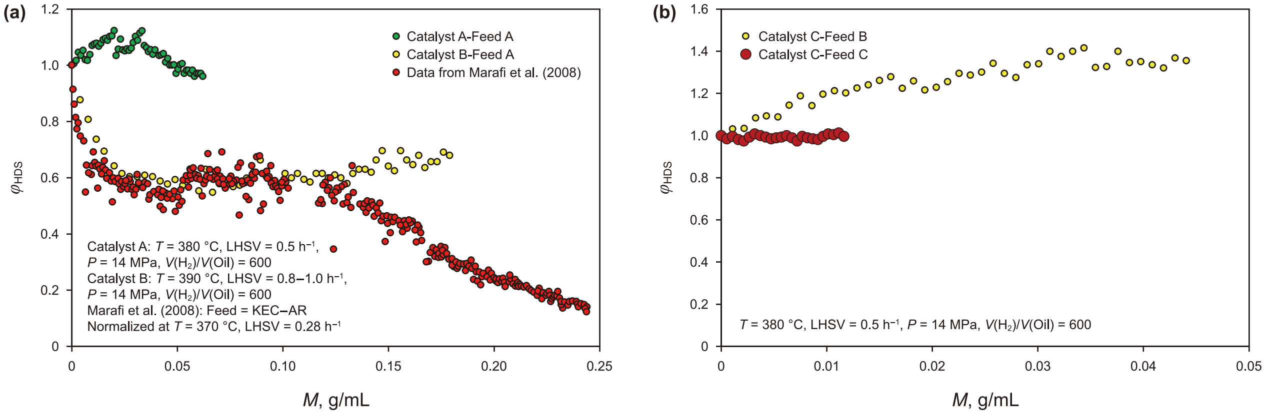

Fig. 2. Plots of HDS activity coefficients as a function of *M* for different catalyst systems.

the usage efficiency of deposited metal sulfides, resulting in an increasing activity profile due to a higher creation rate of active sites. Moreover, according to the previous research (Marafi et al., 2008), a higher metal content in the feedstock and reaction conditions those favor the HDM reaction could help generate more active sites, which could overcome the initial rapid deactivation and lead to a similar profile as Catalyst A. During the early MOR stage, the deactivation due to coke formation slows down. Additionally, the large surface area available to hold more metal deposits results in a slower loss rate of active sites and a faster creation rate of active sites. These factors can lead to a continuous increase in hydrogenation activity until the available surface area is reduced to a certain value where the loss and creation of active sites equilibrate, resulting in a decrease in the hydrogenation activity. In the EOR stage, the dominant factor contributing to deactivation is the diffusion resistance caused by coke formation and metal deposition, resulting in a rapid decline in activity.

Therefore, it is vital to remember that the autocatalytic effect may be at least partially responsible for the apparent deactivation results during the RHT process (Marafi et al., 2010). A remarkable autocatalytic effect may be observed when the autocatalysis rate promoted by the formation of new active sites exceeds the rate of deactivation caused by the loss of active sites and the increasing diffusion resistance at the SOR stage and/or MOR stage. Conversely, a deactivation profile of "S-type" typically emerges when the autocatalysis rate is always lower than the deactivation rate. Obviously, a flexible catalyst deactivation model for the RHT process should accurately reflect all these mechanisms.

4.2. The deactivation profiles of the proposed model

The proposed deactivation model consists of two mechanisms: variation of active sites and diffusion resistance in the catalyst pores. The former mechanism includes both the loss of active sites due to a number of factors mentioned above and the creation of active sites from the by-product metal sulfides. The latter mechanism is based on the pore blocking by coke formation and metal deposition.

Fig. 4 illustrates the individual and combined behaviors of these two mechanisms. As seen in Fig. 4(a), three profiles due to the variation of active site are obtained by Eq. (10). For the first profile, the activity increased at first with increasing dimensionless MOC, and then decreased at a certain level. For the other two profiles, the fast loss of active sites dominated initially, and then there was either a slow loss or a little rise followed by a fast loss. Furthermore, Fig. 4(b) illustrates the impact of the diffusion resistance on catalyst deactivation, as represented by Eq. (24). Typically, the deactivation caused by the diffusion resistance exhibited a gradual decline during the SOR and MOR stages, followed by a sharp drop in the EOR stage. As the parameter λ_0 increased and the parameter η_0 decreased, the deactivation rates in the SOR and MOR stages both tended to rise. Additionally, Fig. 4(c) demonstrates that the deactivation caused by the diffusion resistance can also be approximated using Eq. (25). Moreover, Fig. 4(d) highlights the versatility of the proposed catalyst deactivation model, as it can simulate both classical S-shaped deactivation curves and curves with evident autocatalytic effects. The latter curves are difficult to simulate with the existing models because the generation of new active sites is

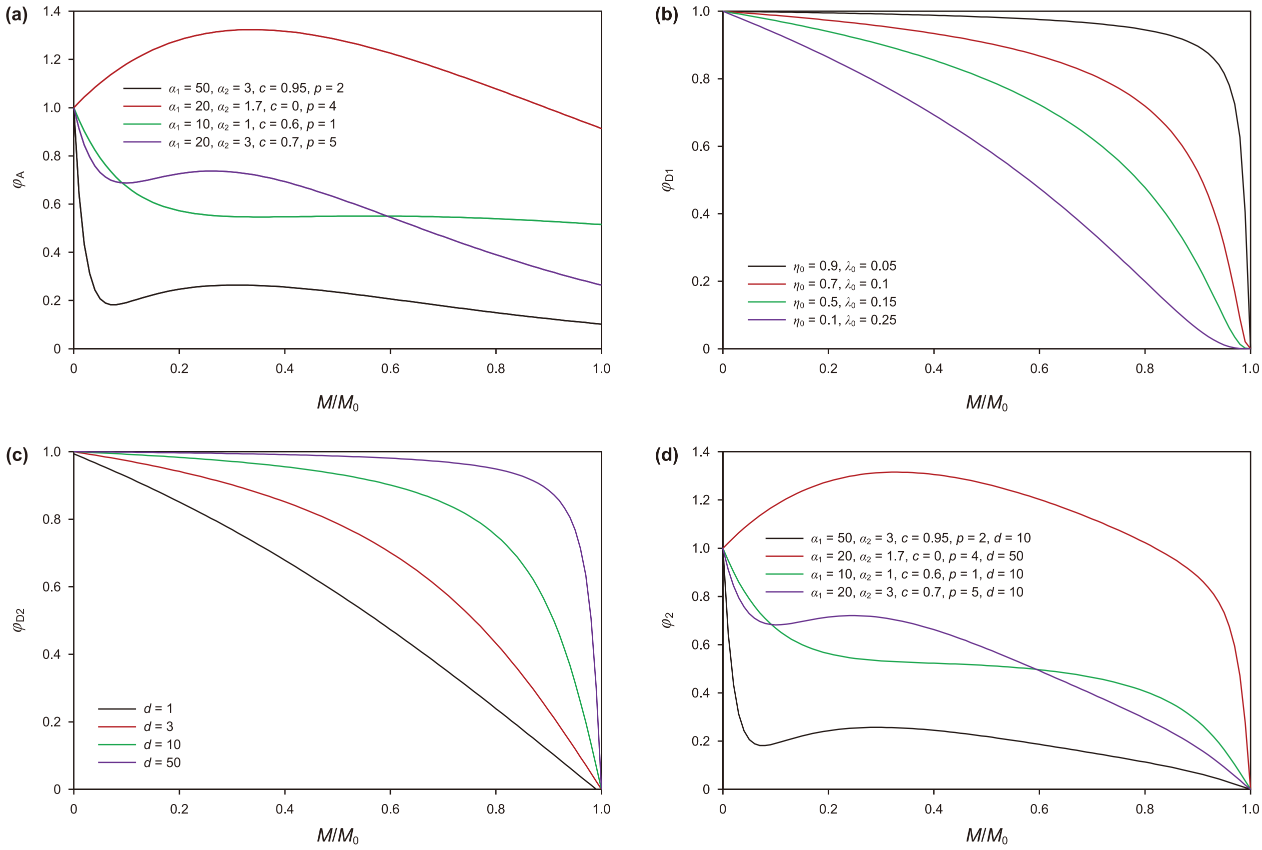

Fig. 4. Plots of the function **(a)** φ_A, **(b)** φ_{D1}, **(c)** φ_{D2}, and **(d)** φ_2 versus M/M_0.

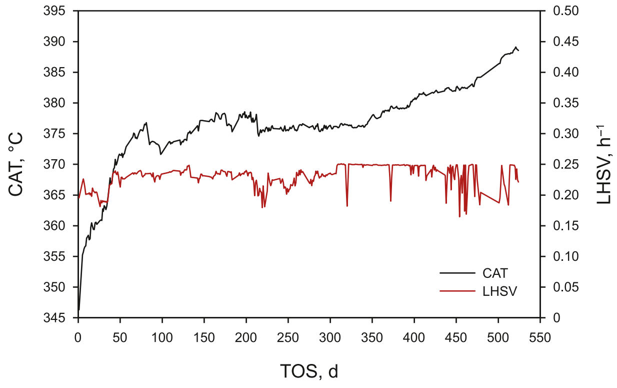

Fig. 5. Plots of CAT and LHSV versus TOS for the industrial unit.

never being taken into account in these models (Marafi et al., 2010). While the proposed mechanism and model appear to effectively reflect the primary factors underlying the catalyst deactivation profiles during RHT processes.

4.3. Simulation of industrial and experimental RHT processes

To investigate the deactivation profile of RHT catalysts, the industrial data from an RHT unit at a Sinopec refinery in China and experimental data from the literature (Marafi et al., 2008) involving a clear autocatalytic effect were chosen and discussed. Figs. 5 and 6 demonstrate the alterations of catalyst average reaction temperature (CAT), liquid hourly space velocity (LHSV), feedstock and product properties, and impurity removal rates over the TOS period for the industrial unit. As depicted in Fig. 5, LHSV remained relatively stable during the operation, while the CAT was adjusted to ensure the desired product qualities. Initially, there was a sharp increase in CAT, followed by a stable or somewhat decreasing CAT during TOS of 80–340 days. Finally, there was a rapid increase in CAT during the last six months. Additionally, as illustrated in Fig. 6, the levels of CCR, sulfur, and nickel in the feedstock remained stable throughout the entire operation period. In contrast, the vanadium content in the feedstock exhibited significant fluctuations over several days. Notably, at the early 200 days, the removal rates of impurities decreased initially and then increased, implying the autocatalytic effect actually imposes a regulation on the process.

To accurately model the above-mentioned trends, Eqs. (33) and (28) were utilized to simulate the industrial and experimental RHT processes, respectively. The resulting parameters for HDCCR, HDS, HDNi, and HDV are displayed in Table 4. In addition, using the method proposed in previous works (Alcázar and Ancheyta, 2007; Félix et al., 2019; Sámano et al., 2020b), the sensitivity analysis of the parameters for the industrial RHT process is shown in Fig. 7. It could be seen that the minimum values of SSE were obtained at 0% perturbation for all the parameters, indicating that the results are globally optimized.

Interestingly, as shown in Table 4, the parameters for different hydrogenation reactions of the industrial process were obviously different. To better evaluate this, the original and predicted deactivation curves of HDCCR, HDS, HDNi, and HDV versus M/M_0 were given, as shown in Fig. 8. As shown in Fig. 8 and Table 4, during the SOR stage, the catalyst deactivation rate increased in the order of HDCCR, HDS, HDNi and HDV, and the diminution rate constants of the type I active site concentration α_1 for these reactions were 14.87, 16.93, 20.43 and 37.20, respectively. Considering the rapid and dominant effect of coking during this stage, α_1 could be mainly determined by the mechanism of coke formation. During the transition region between the SOR stage and the MOR stage, the initial fraction of the type I active site c should play a critical role in

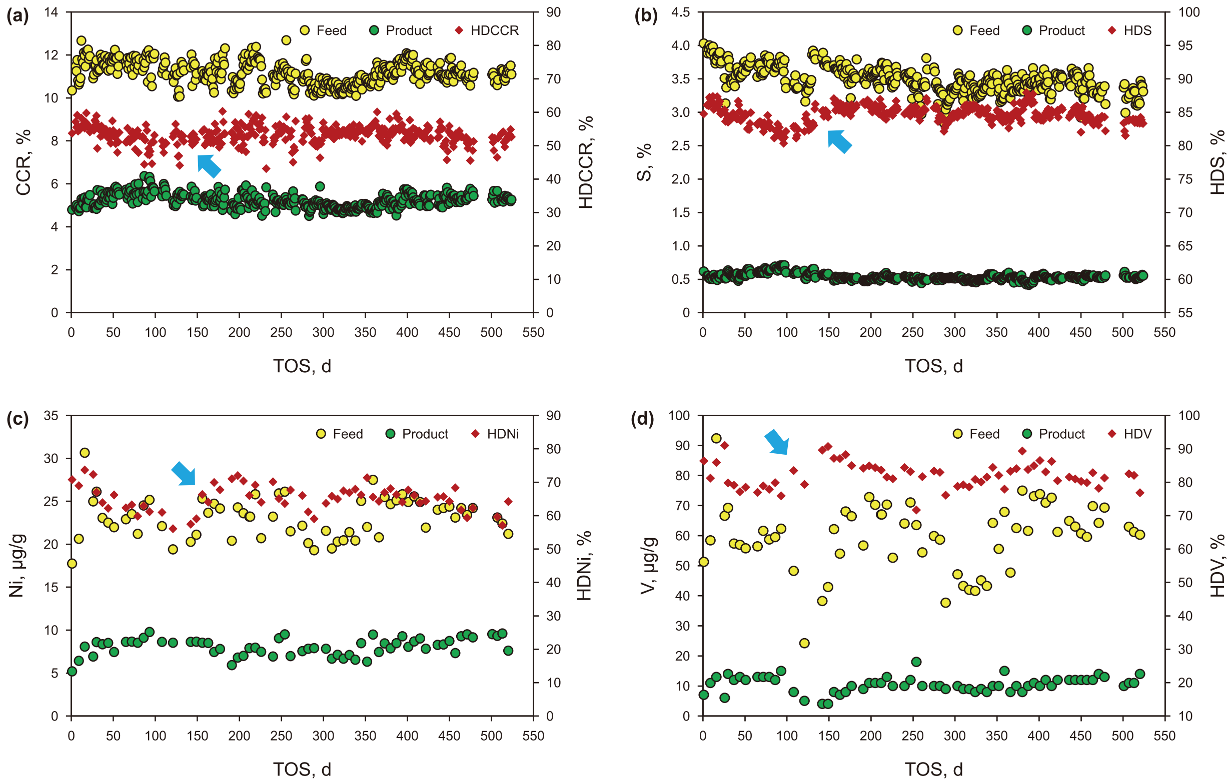

Fig. 6. Plots of **(a)** carbon-residue, **(b)** sulfur, **(c)** nickel and **(d)** vanadium contents in the feeds and products and their corresponding removal rates versus TOS.

Table 4
Optimal parameters of deactivation function and reaction kinetics for the industrial and literature data.

Parameter	Industrial data				Data from Marafi et al. (2008)
	HDCCR	HDS	HDNi	HDV	HDS
α_1	14.87	16.93	20.43	37.20	30.44
α_2	1.53	1.76	0.14	4.12×10^{-10}	1.85
c	0.999	0.999	0.718	0.540	0.649
p	2.50	2.75	0.96	0.29	3.18
d	2.82	4.53	1.65	4.19	1.14
M_0, g/mL	0.221	0.216	0.212	0.208	0.172
n	2.50	2.50	1.42	1.26	–
E, kJ/mol	121.8	119.6	91.8	87.4	–
A_0	1.30×10^8	3.44×10^9	4.42×10^6	3.69×10^6	–

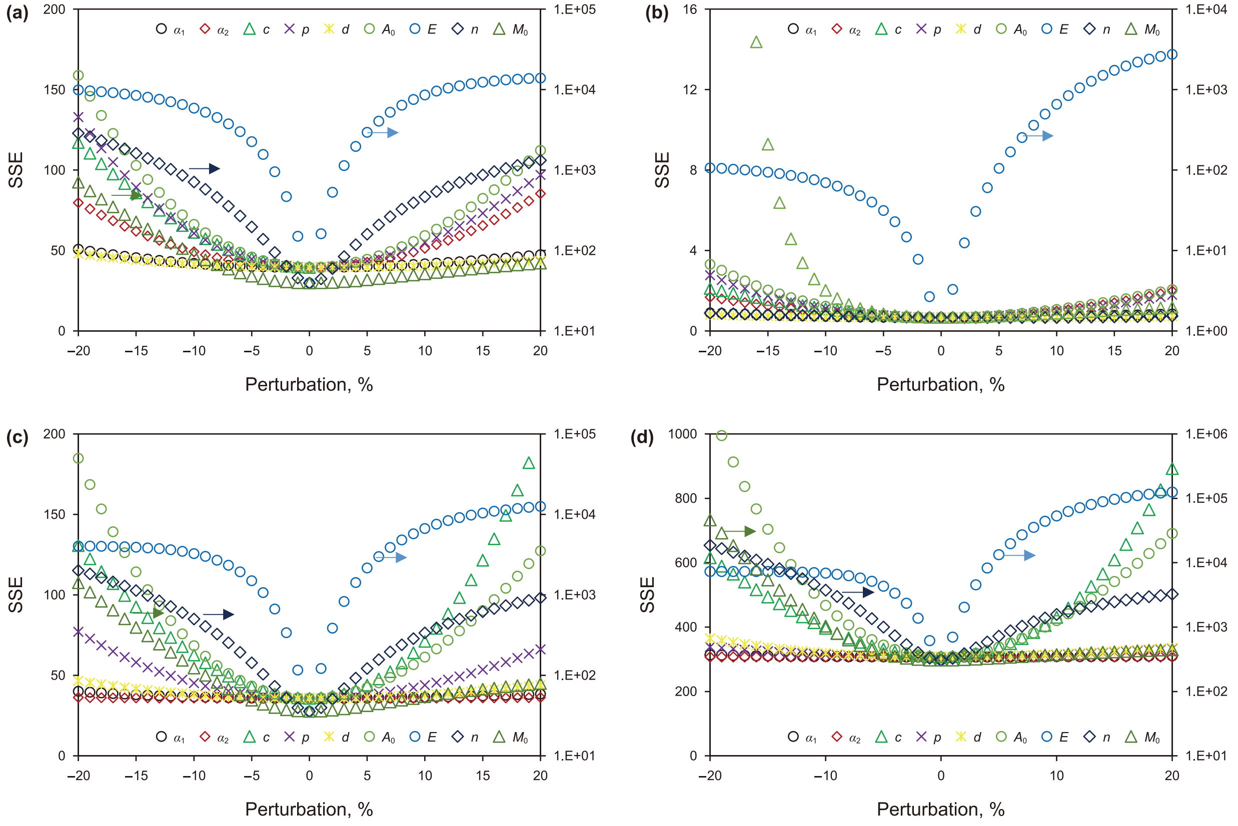

Fig. 7. Plots of the parameter sensitivity analysis for **(a)** HDCCR, **(b)** HDS, **(c)** HDNi and **(d)** HDV.

determining the activity coefficient φ. However, although φ usually decrease with increasing c, it does not decrease to near zero when even c is close to 1. This is because in the proposed model, the generated active sites from deposited metals are treated as type II active sites and they mix together with the original type II active sites as shown in the last term of Eq. (10). Thus, when the value of c approaches 1, there are still some type II active sites present. In this case, though the c values for HDCCR, HDS, HDNi, and HDV were 0.999, 0.999, 0.718, and 0.540 respectively. However, the values of φ during the transition region between the SOR stage and the MOR stage were close due to the different generation rates of type II active sites, as shown in Fig. 8. During the MOR stage, there was a clear increase in activity for HDCCR, HDS, and HDNi, which can be attributed to the autocatalytic effect (Al-Dalama et al., 2014; Marafi et al., 2008, 2010). However, the impact on HDV was very weak. In other words, the autocatalytic effect on different hydrogenation reactions is different, which is consistent with other researches (Al-Dalama et al., 2014; Filby and Branthaver, 1987; Marafi et al., 2010) and our experiments. In the proposed model, the parameter p determined the generation rate of the equivalent type II active site, while the parameter α_2 determined the diminution rate of type II active site. These two parameters worked together to determine the morphology of φ during the MOR stage. Considering the dominant effect of metal deposition during this stage, these two parameters could be determined by the deactivation mechanism of metal deposition. As shown in Table 4 and Fig. 8, the parameters p and α_2 both decreased in the order of HDS, HDCCR, HDNi and HDV, resulting in flatter deactivation profiles in the same order. It should be noted that the α_2 value was only 0.14 for HDNi and was even close to zero for HDV, indicating that the HDNi and HDV reactions are not sensitive to active site concentration during this stage. Research has demonstrated that the activity of HDM is mainly dependent on the pore diameter (Liu et al., 2016; Oyekunle et al., 2005; Oyekunle and Ikpekri, 2004). During the EOR stage, the

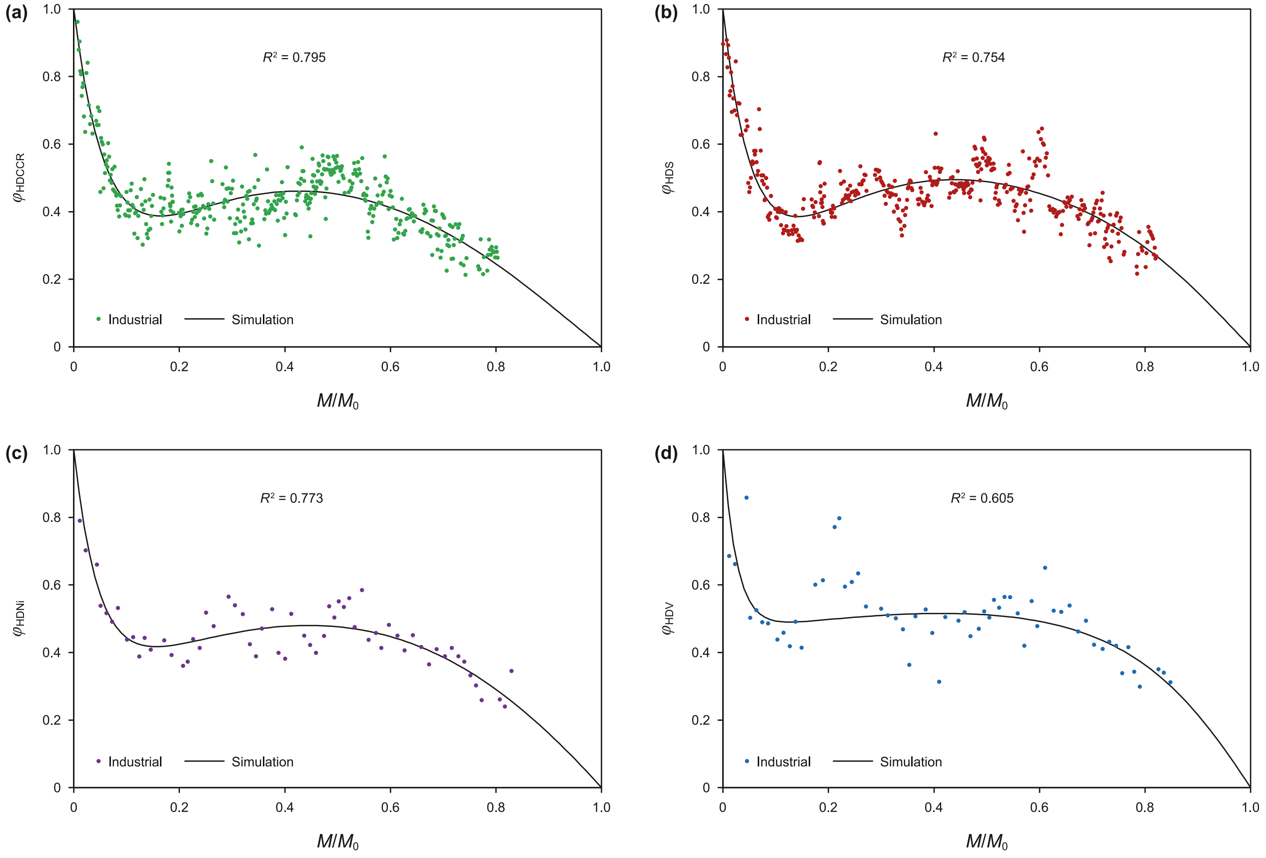

Fig. 8. Plots of the industrial and simulated deactivation profiles versus M/M_0 for **(a)** HDCCR, **(b)** HDS, **(c)** HDNi and **(d)** HDV.

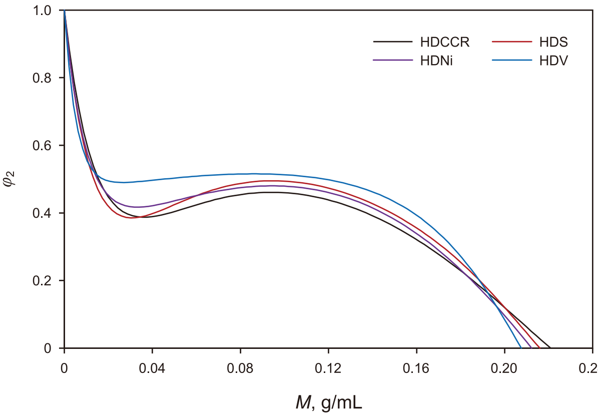

Fig. 9. Plots of the simulated deactivation profiles versus M for HDCCR, HDS, HDNi and HDV.

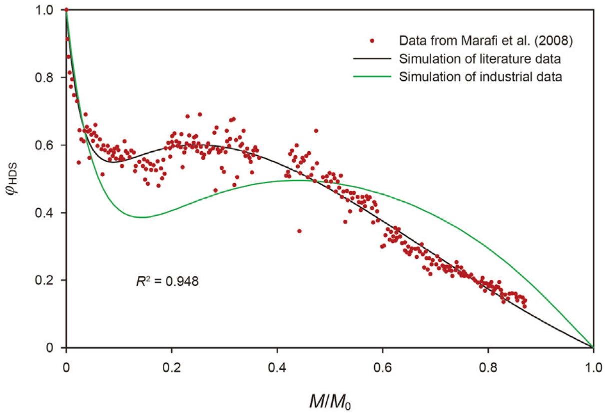

Fig. 10. Plots of the original and simulated deactivation profiles versus M/M_0 for HDS of the industrial unit and experiments from the literature (Marafi et al., 2008).

rate of catalyst deactivation due to diffusion resistance increased in the following order: HDNi, HDCCR, HDV, and HDS. This trend was influenced by both coke formation and metal deposition, which is indicated by the parameter d in the proposed model. Moreover, the proposed model effectively simulated the deactivation profiles of different hydrogenation reactions, with R^2 values of 0.795, 0.754, 0.773, and 0.605 for HDCCR, HDS, HDNi, and HDV, respectively. The low R^2 value observed for HDV could be attributed to the significant fluctuation of vanadium content in the feedstock, as the feedstock properties were not included in the reaction kinetic model. In addition, as depicted in Fig. 9, the deactivation curves of HDCCR, HDS, and HDNi were remarkably alike, with slightly differences in the values of M_0 ranging from 0.208 to 0.221 g/mL. These values seemed reasonable for the accumulated MOC calculated by Eq. (29) was 0.177 g/mL for the industrial unit. It should be noted that HDV exhibited higher activity during the MOR stage compared to HDNi, it demonstrated a more rapid deactivation during EOR stage, thus yielding a lower M_0 value. This observation is consistent with the reactivity of vanadium, which tends to deposit on the pore mouth and results in the greater diffusion resistance during the EOR stage despite its higher reactivity (Marafi et al., 2010).

To gain a deeper insight into the catalyst deactivation behavior with the autocatalytic effect, Fig. 10 displays the experimental and simulated deactivation profiles for the HDS process from the literature (Marafi et al., 2008), as well as the simulated deactivation profile for the HDS process in the aforementioned industrial unit. It is worth noting that the proposed model accurately simulated the HDS data from the literature, achieving a highly satisfactory R^2 value of 0.948. Additionally, the deactivation behaviors in these two processes differed significantly, despite both indicating the clear autocatalytic effect. Specifically, the maximum value of the HDS activity coefficient during the MOR stage for the industrial unit was observed at an M/M_0 value of approximately 0.44, while the corresponding value for the experimental HDS data was approximately 0.25. As suggested above, it is reasonable to speculate that the autocatalytic effect is not only related to different hydrogenation reactions, but are also influenced by the catalyst system, feedstock properties, and reaction conditions. Specifically, as suggested by Eq. (10), whether there is a clear autocatalytic effect during the RHT process is mainly determined by the relative rate of creation and loss of active sites. A highly stable catalyst system, a residue with higher reactivity and reaction conditions that favors catalyst activity stability may result in a longer absence of clear autocatalytic effects.

To further highlight the suggested model's flexibility, the original and simulated impurity concentrations of the industrial unit products are compared in Fig. 11. It is evident that the simulated impurity contents, which had narrower fluctuation ranges, closely tracked the changing pattern of product impurity contents. Regardless of the fluctuation of reaction conditions, the simulation of an industrial unit is still a great challenge due to the fluctuation of feed properties, which would somehow affect the reaction kinetics. It is possible to accept that there are some residuals between the simulated and industrial data because the reaction kinetics in this work did not account for the influence of feedstock properties. Fig. 12 shows the difference between the simulated and expected removal rates for different hydrogenation reactions. It can be seen that the difference was mostly below 10% for HDCCR and HDNi, while it was mostly below 5% for HDS and HDV.

Overall, despite the complexity of the catalyst deactivation mechanisms involved, the proposed model appears to effectively reflect the primary factors underlying the catalyst deactivation profiles during the RHT process. Specifically, this model accurately describes the deactivation mechanisms considering the loss of active sites, the diffusion resistance, and the critical role of autocatalysis from the generation of new active sites at the same time. As a result, the proposed model has demonstrated significant adaptability during experimental and industrial RHT processes, which can exhibit different types of deactivation profiles depending on the strength of the autocatalytic effect.

While the model being proposed displays potential, additional work is needed to validate its adaptability and improve its predictive capabilities. This study only focused on testing the proposed model in combination with reaction kinetics, or on its own. Future research should explore combining the deactivation model with a reactor model. In addition, the deactivation models given by Eqs. (27) and (28) contain seven and six parameters respectively. When integrated with the reaction kinetics given by Eqs. (32) and (33), an additional two or three parameters are introduced, presenting a formidable challenge for global optimization of a highly non-linear function with such a large parameter space. It is highly advisable, whenever possible, to prioritize the fitting of the reaction kinetics parameters first, using the available data. Regardless, a careful

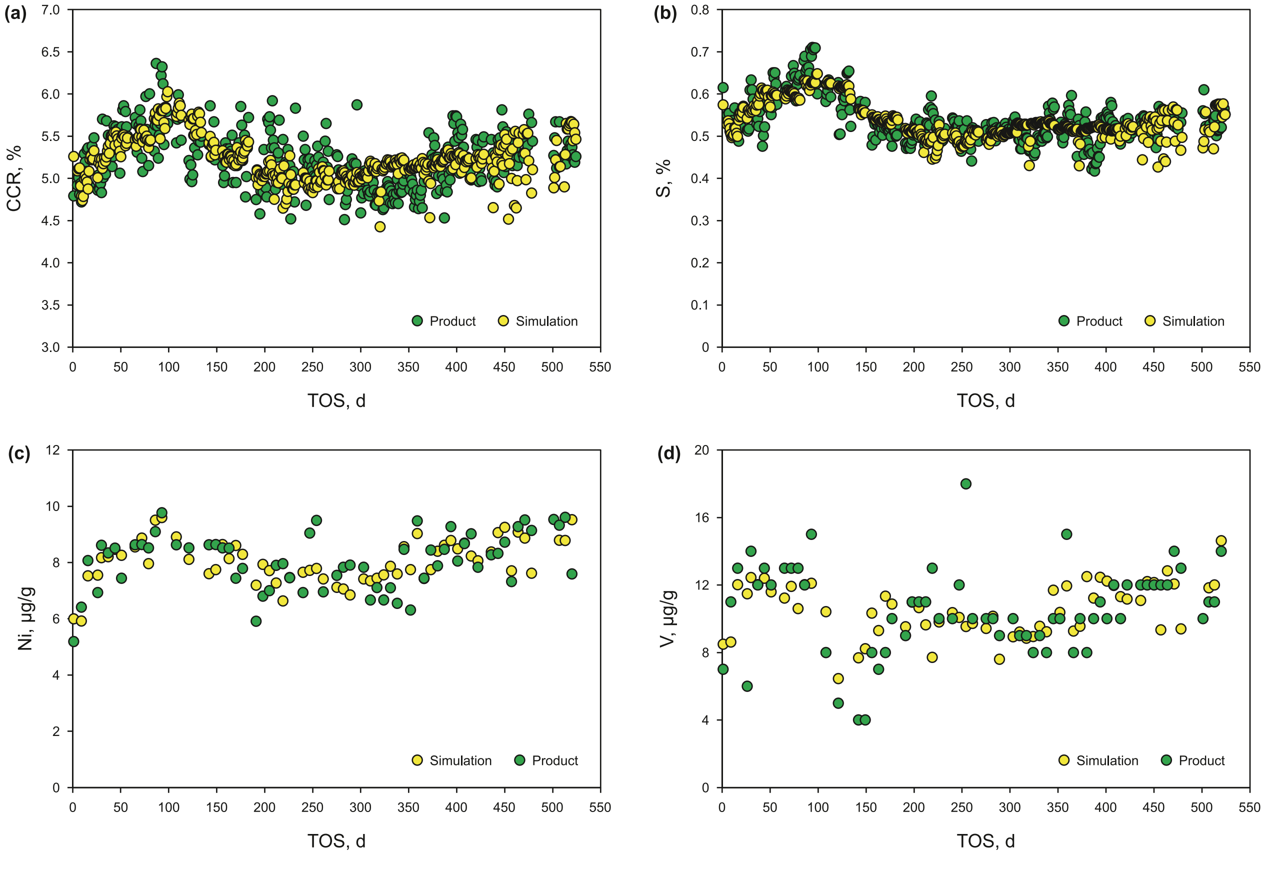

Fig. 11. Plots of **(a)** carbon-residue, **(b)** sulfur, **(c)** nickel and **(d)** vanadium contents and their simulated values versus TOS.

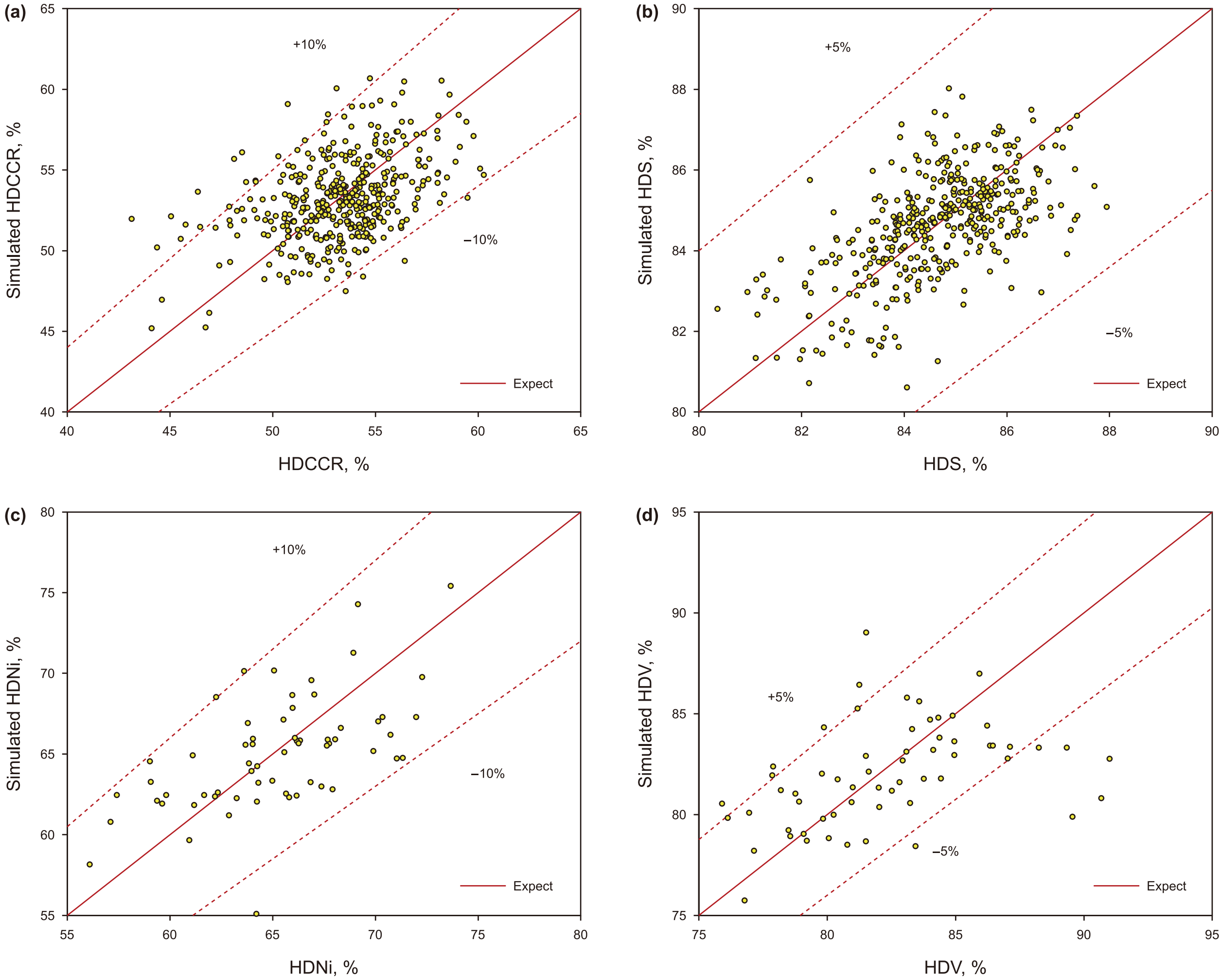

Fig. 12. Plots of industrial and simulated **(a)** HDCCR, **(b)** HDS, **(c)** HDNi and **(d)** HDV ratios.

selection of initial parameter values coupled with a rigorous sensitivity analysis of the fitted parameters is paramount to ensure the robustness and reliability of the model results. Furthermore, we believe that catalyst systems, feedstock properties, and reaction conditions may lead to different contributions of various deactivation factors to the deactivation profile, particularly leading to the difference in the dominant deactivation factors, which in turn will weaken autocatalysis to different degrees and ultimately pose great challenges to the predictive accuracy of the proposed model. Therefore, it is necessary to collect experimental and industrial data under different reaction scenarios and to constantly revise the model to obtain a more accurate and reliable prediction.

5. Conclusions

A remarkable autocatalytic effect was found at the SOR and/or MOR stages of the RHT process, which originated from the formation of new active sites from the deposited metal sulfides. This effect results in significantly distinct deactivation profiles from the conventional "S-shaped" one. By considering this effect together with a number of deactivation influencing factors such as active site formation from by-product metal sulfides, deactivation due to active site coverage by coke formation and metal deposition, active site poisoning by highly-adsorbed species, active phase sintering, and the diffusion resistance due to pore blockage by coke formation and metal deposition, a three-stage deactivation model was proposed. The proposed model proved to be very versatile, being able to simulate both classical "S-shaped" deactivation curves and curves with obvious autocatalytic effects. With the help of the proposed model, it is able to accurately track the whole deactivation curves, as well as predict the product properties, operating mode, and operational cycle of an RHT unit. Further investigations are needed to improve the predictive capabilities of the proposed model and to maximize the autocatalytic effect during the RHT process.

CRediT authorship contribution statement

Zhong-Huo Deng: Writing – original draft, Methodology, Investigation, Conceptualization. **Rong Shi:** Investigation. **Liang Ren:** Investigation. **Xin-Peng Nie:** Investigation. **Qiang Fang:** Investigation. **Zhen Wang:** Investigation. **Wei Han:** Writing – review & editing. **Li-Shun Dai:** Resources, Investigation.

Declaration of competing interest

The authors declare that they have no known competing financial interests or personal relationships that could have appeared to influence the work reported in this paper.

Acknowledgement

The authors gratefully acknowledge financial supports by the National Key Research and Development Program of China (2021YFA1501204) and the project of SINOPEC RIPP Co. Ltd (PR20230230).

Appendix A. Supplementary data

Supplementary data to this article can be found online at https://doi.org/10.1016/j.petsci.2025.04.031.

Nomenclature

Symbols	
A	proportional constant in Eq. (16)
A_0	initial pre-exponential factor
c	initial fraction of type I active sites
C	impurity content, μg/g or %
d	proportional constant in Eq. (25)
D	diffusion coefficient within pore catalyst, m^2/s
E	apparent activation energy, J/mol
F_L	feed flow rate, m^3/h
k	reaction rate constant
L	length of catalyst pores, mm
LHSV	liquid hourly space velocity, h^{-1}
M	concentration of metals-on-catalyst, g/mL
M_0	maximum concentration of metals-on-catalyst, g/mL
M_i	concentration of metals-on-catalyst at time-on-stream i, g/mL
n	reaction order
N	total concentration of active sites for any particular reaction
N_1	concentration of type I active sites
N_2	concentration of type II active sites
p	proportional constant in Eq. (10)
p_1	generation rate constant of the equivalent type II active sites
r_0	initial catalyst pore radius, nm
r_m	hydrodynamic radius of reactant, nm
r_τ	catalyst pore radius at a given dimensionless concentration of metals-on-catalyst, nm
R	the gas constant, 8.314 J/(mol·K)
SSE	the sum of squares errors
t_i	time-on-stream interval i, h
T	reaction temperature, K
V_{cat}	loading volume of catalyst, m^3
Superscripts and subscripts	
0	initial condition
cal	simulated data
ind	industrial data
exp	experimental data
f	feed
Ni	nickel
p	product
V	vanadium
τ	condition at a given dimensionless metals-on-catalyst
Greek letters	
α_1	diminution rate constant of type I active sites concentration
α_2	diminution rate constant of type II active sites concentration
η	overall effectiveness factor
λ	the ratio of the reactant radius to the catalyst pore radius
ρ_L	feed density, kg/m^3
ρ_M	density of the deposited metals, g/mL
τ	dimensionless concentration of metals-on-catalyst
φ	overall activity coefficient
φ_A	deactivation function due to variation of active sites
φ_D	deactivation function due to deposits
ϕ	Thiele modulus

References

Al Bazzaz, H., Kang, J.L., Chehadeh, D., Bahzad, D., Wong, D.S.H., Jang, S.S., 2015. Robust predictions of catalyst deactivation of atmospheric residual desulfurization. Energy Fuels 29, 7089–7100. https://doi.org/10.1021/acs.energyfuels.5b01841.

Alcázar, L.A., Ancheyta, J., 2007. Sensitivity analysis based methodology to estimate the best set of parameters for heterogeneous kinetic models. Chem. Eng. J. 128, 85–93. https://doi.org/10.1016/J.CEJ.2006.10.012.

Al-Dalama, K.M., Stanislaus, A., Navvamani, R., Al-Marri, M., Furimsky, E., 2014. Evidence for autocatalysis and its implications for the kinetics of hydroprocessing of petroleum residues. Petrol. Sci. Technol. 32, 862–869. https://doi.org/10.1080/10916466.2011.609493.

Al-Mutairi, A., Marafi, A., 2012. Effect of the operating pressure on residual oil hydroprocessing. Energy Fuels 26, 7257–7262. https://doi.org/10.1021/ef3011228.

Bahzad, D., Kam, E., 2009. Atmospheric residues of Kuwait heavy crude upgrading: a pilot plant and model simulation study. Energy Fuels 23, 1683–1694. https://doi.org/10.1021/ef800963t.

Barré, L., Simon, S., Palermo, T., 2008. Solution properties of asphaltenes. Langmuir 24, 3709–3717. https://doi.org/10.1021/la702611s.

Beck, R.E., Schultz, J.S., 1972. Hindrance of solute diffusion within membranes as measured with microporous membranes of known pore geometry. Biochim. Biophys. Acta Biomembr. 255, 273–303. https://doi.org/10.1016/0005-2736(72)90028-4.

Centeno, G., Ancheyta, J., Alvarez, A., Marroquín, G., Alonso, F., Castillo, A., 2012. Effect of different heavy feedstocks on the deactivation of a commercial hydrotreating catalyst. Fuel 100, 73–79. https://doi.org/10.1016/j.fuel.2012.01.027.

Chehadeh, D., Albazzaz, H., Bahzad, D., 2018. Predicted effects of heavy feeds on the deactivation of a commercial atmospheric residue desulfurization catalyst system. Energy Fuels 32, 5480–5488. https://doi.org/10.1021/acs.energyfuels.7b04058.

Chehadeh, D., Khajah, M., Albazzaz, H., Bahzad, D., 2021. Effect of catalyst and feed properties on the deactivation parameters of an ARDS process model for HDS and HDM reactions. Chem. Eng. Commun. 208, 1725–1736. https://doi.org/10.1080/00986445.2020.1813118.

Chehadeh, D., Ma, X., Al Bazzaz, H., 2023. Recent progress in hydrotreating kinetics and modeling of heavy oil and residue: a review. Fuel 334, 126404. https://doi.org/10.1016/j.fuel.2022.126404.

Chen, K., Cao, Y., Zhu, H., Ge, H., Yang, T., Zhou, Z., Cheng, Z., 2022. Experimental determination on the deactivation kinetics of residue hydroprocessing in a two-stage fixed bed loaded with HDM and HDS catalysts. Processes 10, 1822. https://doi.org/10.3390/pr10091822.

Chen, Z., Liu, J., Wu, Y., Xu, Z., Liu, X., Zhao, S., Xu, C., 2015. Polydisperse size distribution of monomers and aggregates of sulfur-containing compounds in petroleum residue fractions. Energy Fuels 29, 4730–4737. https://doi.org/10.1021/acs.energyfuels.5b00418.

Chen, Z., Zhao, S., Xu, Z., Gao, J., Xu, C., 2011. Molecular size and size distribution of petroleum residue. Energy Fuels 25, 2109–2114. https://doi.org/10.1021/ef200128m.

Corella, J., Monzón, A., 1988. Modeling of the deactivation kinetics of solid catalysts by two or more simultaneous and different causes. Ind. Eng. Chem. Res. 27, 369–374. https://doi.org/10.1021/ie00075a001.

Dejonghe, S., Hubaut, R., Grimblot, J., Bonnelle, J.P., Des Courieres, T., Faure, D., 1990. Hydrodemetallation of a vanadylporphyrin over sulfided Ni-Mo-γAl_2O_3, Mo-γAl_2O_3, and γAl_2O_3 catalysts - effect of the vanadium deposit on the toluene hydrogenation. Catal. Today 7, 569–585. https://doi.org/10.1016/0920-5861(90)80009-E.

Deng, Z., Dai, L., Han, W., Cai, X., Nie, X., Fang, Q., Nie, H., 2022. Towards a deep understanding of the evolution and molecular structures of refractory sulfur compounds during deep residue hydrotreating process. Fuel Process. Technol. 231, 107235. https://doi.org/10.1016/j.fuproc.2022.107235.

Elizalde, I., Ancheyta, J., 2014a. Modeling the deactivation by metal deposition of heavy oil hydrotreating catalyst. Catal. Today 220–222, 221–227. https://doi.org/10.1016/j.cattod.2013.04.008.

Elizalde, I., Ancheyta, J., 2014b. Application of a three-stage approach for modeling the complete period of catalyst deactivation during hydrotreating of heavy oil. Fuel 138, 45–51. https://doi.org/10.1016/j.fuel.2014.02.073.

Elizalde, I., Ancheyta, J., 2014c. Modeling catalyst deactivation during hydrocracking of atmospheric residue by using the continuous kinetic lumping model. Fuel Process. Technol. 123, 114–121. https://doi.org/10.1016/J.FUPROC.2014.02.006.

Félix, G., Ancheyta, J., Trejo, F., 2019. Sensitivity analysis of kinetic parameters for heavy oil hydrocracking. Fuel 241, 836–844. https://doi.org/10.1016/J.FUEL.2018.12.058.

Filby, R.H., Branthaver, J.F., 1987. Metal complexes in fossil fuels: geochemistry, characterization, and processing. ChemInform 19. https://doi.org/10.1021/bk-1987-0344.

Furimsky, E., Massoth, F.E., 1999. Deactivation of hydroprocessing catalysts. Catal. Today 52, 381–495. https://doi.org/10.1016/S0920-5861(99)00096-6.

Hubaut, R., 2007. Vanadium-based sulfides as hydrotreating catalysts. Appl. Catal. A. Gen. 322, 121–128. https://doi.org/10.1016/j.apcata.2007.01.020.

Idei, K., Takahashi, T., Kai, T., 2003. Estimation of coke and metal deposition distribution within hydrodesulfurization catalyst pore at the last stage of operation. J. Jpn. Petrol. Inst. 46, 45–52. https://doi.org/10.1627/jpi.46.45.

Idei, K., Yamamoto, Y., Takehara, S., 1998. Generalized deactivation equation of catalyst in hydrodesulfurization of light and heavy oils. Kagaku Kogaku Ronbunshu 24, 653–659. https://doi.org/10.1252/kakoronbunshu.24.653.

Idei, K., Yamamoto, Y., Yamazaki, H., 1995. Kinetic model and analysis method of catalyst deactivation in hydrodesulfurization of light and heavy Oils. Kagaku Kogaku Ronbunshu 21, 972–983. https://doi.org/10.1252/kakoronbunshu.21.972.

Jia, Y., Yang, Q., Sun, S., Nie, H., Li, D., 2016. The influence of metal deposits on residue hydrodemetallization catalysts in the absence and presence of coke. Energy Fuels 30, 2544–2554. https://doi.org/10.1021/acs.energyfuels.5b01553.

Jiang, L., Weng, Y., Liu, C., 2010. Hydrotreating residue deactivation kinetics and metal deposition. Energy Fuels 24, 1475–1478. https://doi.org/10.1021/ef9014586.

Jurado, J., Ancheyta, J., 2022. Reactor model for heavy oil hydrotreating with catalyst deactivation based on vanadium and coke deposition. Energy Fuels 36, 11132–11141. https://doi.org/10.1021/acs.energyfuels.2c00876.

Jurado, J., Ancheyta, J., Samano, V., 2024. Application of a deactivation model for hydrotreating of heavy crude oil in bench-scale reactor. Fuel 371, 131665. https://doi.org/10.1016/j.fuel.2024.131665.

Kam, E.K.T., Al-Shamali, M., Juraidan, M., Qabazard, H., 2005. A hydroprocessing multicatalyst deactivation and reactor performance model-pilot-plant life test applications. Energy Fuels 19, 753–764. https://doi.org/10.1021/ef049843s.

Khang, S.J., Mosby, J.F., 1986. Catalyst deactivation due to deposition of reaction products in macropores during hydroprocessing of petroleum residuals. Ind. Eng. Chem. Process Des. Dev. 25, 437–442. https://doi.org/10.1021/i200033a015.

Kohli, K., Prajapati, R., Maity, S.K., Sau, M., Garg, M.O., 2016. Deactivation of hydrotreating catalyst by metals in resin and asphaltene parts of heavy oil and residues. Fuel 175, 264–273. https://doi.org/10.1016/j.fuel.2016.02.036.

Kressmann, S., Morel, F., Harlé, V., Kasztelan, S., 1998. Recent developments in fixed-bed catalytic residue upgrading. Catal. Today 43, 203–215. https://doi.org/10.1016/S0920-5861(98)00149-7.

Liu, T., Ju, L., Zhou, Y., Wei, Q., Ding, S., Zhou, W., Luo, X., Jiang, S., Tao, X., 2016. Effect of pore size distribution (PSD) of Ni-Mo/Al_2O_3 catalysts on the Saudi Arabia vacuum residuum hydrodemetallization (HDM). Catal. Today 271, 179–187. https://doi.org/10.1016/j.cattod.2015.07.045.

Maity, S.K., Pérez, V.H., Ancheyta, J., Rana, M.S., Centeno, G., 2007. Effect of asphaltene contained in feed on deactivation of maya crude hydrotreating catalyst. Petrol. Sci. Technol. 25, 241–249. https://doi.org/10.1080/10916460601054701.

Marafi, A., Almarri, M., Stanislaus, A., 2008. The usage of high metal feedstock for the determination of metal capacity of ARDS catalyst system by accelerated aging tests. Catal. Today 130, 395–404. https://doi.org/10.1016/j.cattod.2007.10.097.

Marafi, A., Stanislaus, A., Furimsky, E., 2010. Kinetics and modeling of petroleum residues hydroprocessing. Catal. Rev. Sci. Eng. 52, 204–324. https://doi.org/10.1080/01614941003720167.

Marafi, M., Stanislaus, A., 2001. Influence of catalyst acidity and feedstock quality on hydrotreating catalyst deactivation by coke deposition. Petrol. Sci. Technol. 19, 697–710. https://doi.org/10.1081/LFT-100105284.

Martínez, J., Ancheyta, J., 2012. Kinetic model for hydrocracking of heavy oil in a CSTR involving short term catalyst deactivation. Fuel 100, 193–199. https://doi.org/10.1016/J.FUEL.2012.05.032.

Melkote, R.R., Jensen, K.F., 1989. Models for catalytic pore plugging: application to hydrodemetallation. Chem. Eng. Sci. 44, 649–663. https://doi.org/10.1016/0009-2509(89)85041-9.

Morales–Leal, F.J., Ancheyta, J., Torres–Mancera, P., Alonso, F., 2023. Experimental methodologies to perform accelerated deactivation studies of hydrotreating catalysts. Fuel 332, 126074. https://doi.org/10.1016/J.FUEL.2022.126074.

Oyekunle, L.O., Ikpekri, O.B., 2004. Modeling of hydrodesulfurization catalysts. I. Influence of catalyst pore structures on the rate of demetallization. Ind. Eng. Chem. Res. 43, 6647–6653. https://doi.org/10.1021/ie049618y.

Oyekunle, L.O., Ikpekri, O.B., Jaiyeola, A., 2005. Modelling of hydrodesulfurization catalysts: II. Effects of catalyst pore structures on deactivation by metal deposits. Catal. Today 109, 128–134. https://doi.org/10.1016/j.cattod.2005.08.012.

Perego, C., Peratello, S., 1999. Experimental methods in catalytic kinetics. Catal. Today 52, 133–145. https://doi.org/10.1016/S0920-5861(99)00071-1.

Plasson, R., Brandenburg, A., Jullien, L., Bersini, H., 2011. Autocatalyses. J. Phys. Chem. A 115, 8073–8085. https://doi.org/10.1021/jp110079p.

Rodríguez, E., Félix, G., Ancheyta, J., Trejo, F., 2018. Modeling of hydrotreating catalyst deactivation for heavy oil hydrocarbons. Fuel 225, 118–133. https://doi.org/10.1016/j.fuel.2018.02.085.

Sahu, R., Song, B.J., Im, J.S., Jeon, Y.P., Lee, C.W., 2015. A review of recent advances in catalytic hydrocracking of heavy residues. J. Ind. Eng. Chem. 27, 12–24. https://doi.org/10.1016/j.jiec.2015.01.011.

Sámano, V., Rana, M.S., Ancheyta, J., 2020a. An easy approach based on textural properties to evaluate catalyst deactivation during heavy oil hydrotreating. Catal. Commun. 133, 105823. https://doi.org/10.1016/J.CATCOM.2019.105823.

Sámano, V., Tirado, A., Félix, G., Ancheyta, J., 2020b. Revisiting the importance of appropriate parameter estimation based on sensitivity analysis for developing kinetic models. Fuel 267, 117113. https://doi.org/10.1016/j.fuel.2020.117113.

Seki, H., Yoshimoto, M., 2001. Deactivation of HDS catalyst in two-stage RDS process II. Effect of crude oil and deactivation mechanism. Fuel Process. Technol. 69, 229–238. https://doi.org/10.1016/S0378-3820(00)00143-0.

Sie, S.T., 2001. Consequences of catalyst deactivation for process design and operation. Appl. Catal. A. Gen. 212, 129–151. https://doi.org/10.1016/S0926-860X(00)00851-6.

Takahashi, T., Higashi, H., Kai, T., 2005. Development of a new hydrodemetallization catalyst for deep desulfurization of atmospheric residue and the effect of reaction temperature on catalyst deactivation. Catal. Today 104, 76–85. https://doi.org/10.1016/j.cattod.2005.03.025.

Trueba, D., Palos, R., Bilbao, J., Arandes, J.M., Gutiérrez, A., 2023. Kinetic modeling of the hydrocracking of polystyrene blended with vacuum gasoil. Chem. Eng. J. 451, 138709. https://doi.org/10.1016/j.cej.2022.138709.

Torres-Mancera, P., Ancheyta, J., Martínez, J., 2018. Deactivation of a hydrotreating catalyst in a bench-scale continuous stirred tank reactor at different operating conditions. Fuel 234, 326–334. https://doi.org/10.1016/J.FUEL.2018.06.122.

Torres-Mancera, P., Rayo, P., Ancheyta, J., Marroquín, G., Centeno, G., Alonso, F., 2014. Catalyst deactivation pattern along a residue hydrotreating bench-scale reactor. Catal. Today 220–222, 153–158. https://doi.org/10.1016/j.cattod.2013.10.024.

Toulhoat, H., Hudebine, D., Raybaud, P., Guillaume, D., Kressmann, S., 2005. THERMIDOR: a new model for combined simulation of operations and optimization of catalysts in residues hydroprocessing units. Catal. Today 109, 135–153. https://doi.org/10.1016/j.cattod.2005.08.023.

Zhang, L., Seaton, N.A., 1996. Simulation of catalyst fouling at the particle and reactor levels. Chem. Eng. Sci. 51, 3257–3272. https://doi.org/10.1016/0009-2509(95)00388-6.

Zhang, K., Nie, H., Dai, L., 2021. Application of a new catalyst deactivation model for residue hydrotreating. China Pet. Process. Petrochem. Technol. 23, 11–20. http://www.chinarefining.com/EN/Y2021/V23/I2/11.

Zhao, J., Liu, T., Han, W., Ren, L., Zhang, L., Dai, L., Li, D., 2021. An insight into the molecular structure of sulfur compounds and their reactivity during residual oil hydroprocessing. Fuel 283, 119334. https://doi.org/10.1016/j.fuel.2020.119334.

Zhao, J., Ren, L., Liu, T., Dai, L., Zhang, L., Han, W., Li, D., 2020. An insight into the evolution of sulfur species during the integration process of residue hydrotreating and delayed coking. Ind. Eng. Chem. Res. 59, 12719–12728. https://doi.org/10.1021/acs.iecr.0c02036.